Nano Research 2017, 10(4): 1213–1222
DOI 10.1007/s12274-016-1300-x
Research Article
ISSN 1998-0124
CN 11-5974/O4

A Prussian blue route to nitrogen-doped graphene aerogels as efficient electrocatalysts for oxygen reduction with enhanced active site accessibility

Yayuan Liu[1], Haotian Wang[2], Dingchang Lin[1], Jie Zhao[1], Chong Liu[1], Jin Xie[1], and Yi Cui[1,3] (✉)

[1] *Department of Materials Science and Engineering, Stanford University, Stanford, CA 94305, USA*
[2] *Department of Applied Physics, Stanford University, Stanford, CA 94305, USA*
[3] *Stanford Institute for Materials and Energy Sciences, SLAC National Accelerator Laboratory, 2575 Sand Hill Road, Menlo Park, CA 94025, USA*

Received: 16 August 2016
Revised: 15 September 2016
Accepted: 23 September 2016

KEYWORDS
oxygen reduction reaction,
Prussian blue nanoparticles,
reduced graphene oxide aerogel,
nitrogen doping

ABSTRACT

Developing high-performance nonprecious-metal electrocatalysts for the oxygen reduction reaction (ORR) is crucial for a variety of renewable energy conversion and storage systems. Toward that end, rational catalyst design principles that lead to highly active catalytic centers and enhanced active site accessibility are undoubtedly of paramount importance. Here, we used Prussian blue nanoparticles to anchor Fe/Fe_3C species to nitrogen-doped reduced graphene oxide aerogels as ORR catalysts. The strong interaction between nanosized Fe_3C and the graphitic carbon shell led to synergistic effects in the ORR, and the protection of the carbon shell guaranteed stability of the catalyst. As a result, the aerogel electrocatalyst displayed outstanding activity in the ORR on par with the state-of-the-art Pt/C catalyst at the same mass loading in alkaline media, good performance in acidic media, and excellent stability and crossover tolerance that rivaled that of the best nonprecious-metal ORR electrocatalysts reported to date.

1 Introduction

The oxygen reduction reaction (ORR) is a crucial process in various energy conversion and storage systems, such as fuel cells and metal-air batteries [1–4]. However, due to the intrinsic sluggish kinetics of the ORR, tremendous research efforts have been devoted toward the development of efficient electrocatalysts. So far, platinum (Pt) and its alloys remain the best catalysts for the ORR [5]; nevertheless, they suffer from various drawbacks including high cost, scarcity, limited durability, and poor resistance to poisoning [6–8]. Therefore, it is critical to search for durable nonprecious-metal ORR catalysts that can rival commercial Pt/C ones.

For the rational design of efficient ORR catalysts, two factors should be considered. First, the intrinsic activity of the active sites needs to be optimized by

Address correspondence to yicui@stanford.edu

tuning the chemical composition of the catalysts as well as interactions between catalytic components. Second, the density of the accessible active sites should be maximized, and the active sites should have a porous architecture to facilitate rapid mass transport of ORR-related species (OH^-, H^+, O_2, H_2O, etc.). In regard to the former aspect, considerable progress has been made in exploring materials with promising intrinsic activities, such as metallic-nanoparticle-anchored carbon [9, 10], heteroatom-doped carbon [11–18], transition-metal oxides [19–22], transition-metal-coordinating macrocyclic compounds [23–25], and pyrolyzed metal/nitrogen/carbon materials (M–N/C) [26]. Notably, M–N/C catalysts with Fe/Co as the metal center exhibit prominent ORR activity comparable to that of Pt/C [27–31]. However, the commonly adopted synthetic method, the direct pyrolysis of a carbon source and Fe/Co-containing salt, can lead to non-uniform distribution and stacking of catalytic species and thus limited accessibility to active sites. Therefore, in order to realize similar catalytic performance as that of Pt/C, the loading of such materials often needs to be several times higher [32, 33].

Herein, we describe the synthesis of an M–N/C catalyst via the pyrolysis of Prussian blue (PB, ferric hexacyanoferrate, $Fe_4[Fe(CN)_6]_3{\cdot}xH_2O$) nanoparticles to give three-dimensional (3D) N-doped graphene aerogels, which possessed both of the abovementioned features. PB, a metal-organic framework (MOF) composed of uniformly distributed metal centers (Fe, Co, etc.) linked through cyanide (CN) ligands, can be an ideal precursor for M–N/C catalysts. The high density of $M–N_4$ coordination moieties will result in rich ORR-active M–N–C centers after pyrolysis [33]. The carbonization of PB affords homogeneously distributed catalytic particles on the nanoscale, which provides considerably more active sites compared to the bulk counterparts [34]. In addition, being a commonly used pigment, PB is inexpensive and easily prepared, offering an economical route towards efficient ORR electrocatalysts [35, 36]. Moreover, as demonstrated in previous studies, the inherent porosity of MOF-derived structures offers numerous micropores and mesopores, which is beneficial in the mass transport of catalytic species [37]. Nevertheless, sintering and agglomeration of MOF-derived particles occur during pyrolysis, probably due to the collapse of the framework at elevated temperatures, and thus the resulting surface area is generally far from ideal [15, 34, 38–40].

To mitigate the agglomeration and maximize the electrochemical surface area (ECSA), in this study, we directly anchored PB nanoparticles on graphene oxide sheets (PB@GO), so that the strong bonding between PB and the GO substrates effectively alleviated particle sintering during the subsequent thermal treatment. Moreover, in order to prevent the restacking of GO sheets induced by pyrolysis, PB@GO was subjected to hydrothermal assembly to yield a 3D hydrogel (PB@GO hydrogel), which gave rise to a monolithic reduced graphene oxide aerogel with a uniform deposition of Fe/Fe_3C nanoparticles (Fe/Fe_3C@rGO) after lyophilization and thermal treatment. The electrocatalyst design not only preserved the chemical and physical advantages of MOF-derived structures, but also combined the unique merits of 3D graphene, including high electrical conductivity and rich accessible macroporosity [41]. Noticeably, on introducing N-containing molecules, N-doped aerogel catalysts (Fe/Fe_3C@N-rGO) with a high degree of graphitization and a hierarchical pore structure (abundant micro/mesopores with interconnected macropores) were obtained. Owing to the high intrinsic activity of the catalytic centers and their remarkably enhanced accessibility, the resulting Fe/Fe_3C@N-rGO catalysts exhibited excellent ORR activity at a low mass loading in alkaline media on a rotating disk electrode (RDE) and carbon fiber paper (CFP). Substantially better stability and methanol tolerance than those of commercial Pt/C was also observed. In addition, when Fe/Fe_3C@N-rGO was subjected to acid leaching to remove unstable species, the catalysts exhibited high activity and durability under acidic conditions. Additional experiments were carried out to investigate the roles of Fe, Fe_3C, and graphitic carbon in the ORR, which revealed synergistic interactions between Fe_3C and graphitic carbon in promoting the catalytic reaction, while the protection of the carbon coating contributed to the stability of the catalyst.

2 Results and discussion

The fabrication of the 3D Fe/Fe_3C@N-rGO aerogel is

illustrated in Fig. 1. The GO-directed nucleation and growth method was adopted to synthesize PB nanocubes with an average edge length of ~200 nm directly anchored on GO sheets (Fig. 1(a) and Fig. S1 in the Electronic Supplementary Material (ESM)). The direct coordination method guaranteed a small crystal size and uniform particle distribution. Moreover, as opposed to physical mixing, strong interactions are established between PB and GO through direct coordination, which can effectively prevent aggregation in the subsequent pyrolysis step [42]. Secondly, PB@GO particles were hydrothermally assembled at 150 °C for 10 h in an acidic medium (to prevent the hydrolysis of PB) in the presence of N-containing molecules (dicyandiamide, DCDA). In this manner, a graphene-based 3D hydrogel was obtained with the simultaneous incorporation of N-containing species into the structure (Fig. 1(b) and Fig. S2 in the ESM). Finally, the hydrogel was dehydrated by freeze-drying, followed by calcination at 800 °C under an argon atmosphere to afford a black monolithic aerogel. Scanning electron microscopy (SEM; Fig. 1(c) and Fig. S3 in the ESM) confirmed that the PB-derived nanoparticles retained their cubic shape after pyrolysis and were evenly distributed in the rGO network. Notably, the aerogel demonstrated rich, interconnected micrometer-sized macropores without severe rGO restacking.

The structure and morphology of the as-prepared Fe/Fe_3C@N-rGO aerogel catalyst was further characterized by transmission electron microscopy (TEM), from which a core–shell structure was clearly observed. The PB-derived core retained a cubic shape with a slightly reduced edge length of ~100 nm (Fig. 2(a)), and the shell displayed distinct lattice fringes with a spacing of 0.34 nm (Fig. 2(b)), which corresponded to the (002) plane of graphitic carbon. X-ray diffraction (XRD) spectroscopy was employed to analyze the composition during the synthetic process (Fig. 2(c)). The XRD spectrum of the PB@GO hydrogel displayed distinctive peaks that were in accord with the standard diffraction peaks of PB (JCPDS 77-1161), indicating that the PB nanocubes remained intact after the hydrothermal assembly. The broad amorphous bump between 20° to 30° in the XRD spectrum of PB@GO was attributed to GO. After pyrolysis, diffraction peaks assigned to Fe and Fe_3C (JCPDS 06-0696 and 89-2867) were observed,

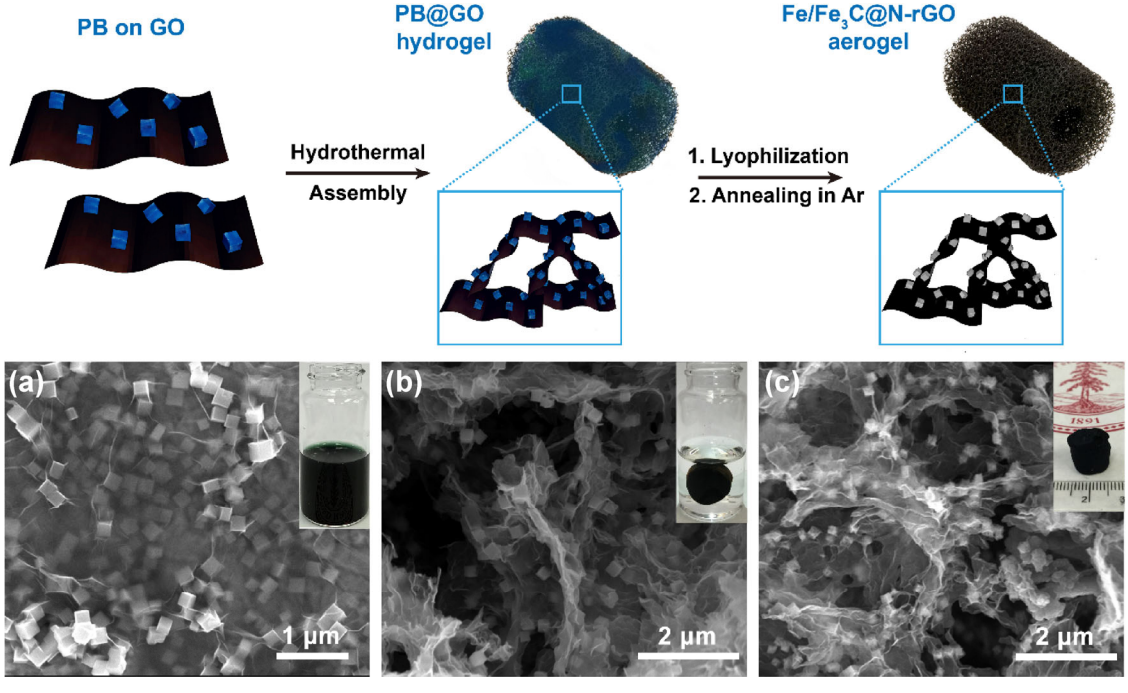

Figure 1 Fabrication process of the 3D Fe/Fe_3C@N-rGO aerogel catalyst. SEM images of (a) the as-synthesized PB@GO, (b) the PB@GO hydrogel obtained via hydrothermal treatment in acidic medium in the presence of DCDA, and (c) the Fe/Fe_3C@N-rGO aerogel catalyst obtained via lyophilization and pyrolysis of the PB@GO hydrogel (insets are the digital camera images of the corresponding states).

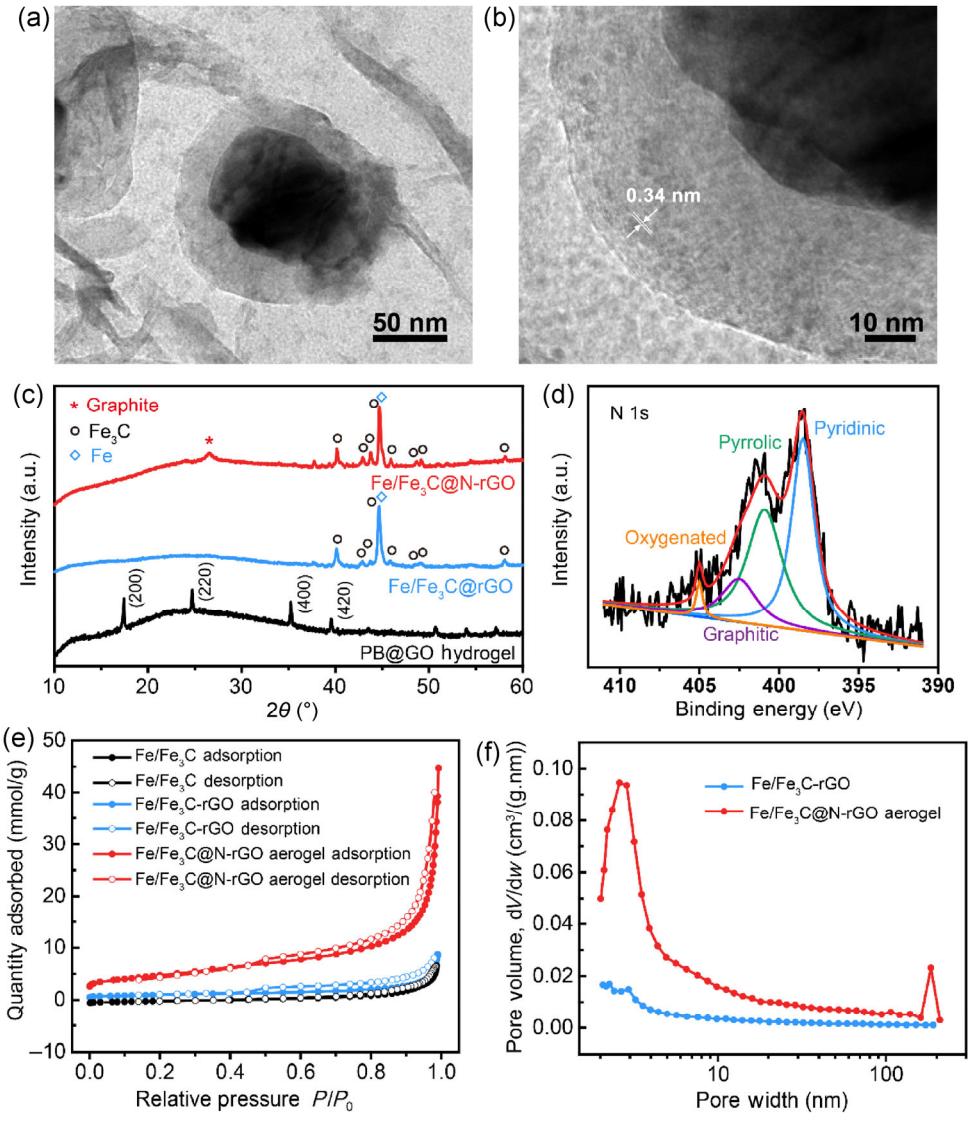

Figure 2 (a) and (b) TEM images of the Fe/Fe_3C@N-rGO aerogel catalyst. (c) XRD spectra of the PB@GO hydrogel, aerogel catalyst without N doping (Fe/Fe_3C@rGO) and aerogel catalyst with N doping (Fe/Fe_3C@N-rGO). (d) High-resolution N 1s XPS spectra of Fe/Fe_3C@N-rGO. (e) N_2 adsorption–desorption isotherms of Fe/Fe_3C, Fe/Fe_3C@N-rGO aerogel, and Fe/Fe_3C-rGO derived from the direct pyrolysis of PB@GO composite. (f) Pore size distribution obtained from the N_2 adsorption–desorption isotherms.

suggesting the complete conversion of PB through the heat treatment. Interestingly, compared to the aerogel obtained without the addition of DCDA during hydrothermal assembly (Fe/Fe_3C@rGO), Fe/Fe_3C@N-rGO exhibited a strong graphitic carbon peak at 26.2°, which was consistent with the TEM observation. This highlighted the indispensable role of DCDA in the formation of a highly graphitized carbon shell [11]. From the aforementioned results, we can conclude that the as-prepared aerogel catalyst was comprised of Fe/Fe_3C nanoparticles encapsulated by a conformal layer of graphitic carbon, which may hamper particle corrosion and agglomeration during ORR. Besides facilitating graphitization, the addition of DCDA also led to the N-doping of the rGO skeleton, as confirmed by X-ray photoelectron spectroscopy (XPS). The XPS survey spectrum (Fig. S4 in the ESM) revealed the elemental composition of N to be ~5.2%, which was relatively high due to the high N content of PB and the incorporation of DCDA. Notably, the surface Fe was only 0.6 at.% as determined by XPS, while the actual Fe/Fe_3C content was determined to be more

than 60 wt.% using thermogravimetric analysis (TGA; Fig. S5 in the ESM). This difference mainly resulted from the shielding of Fe/Fe_3C nanoparticles by the graphitic carbon shells. The high resolution N 1s spectrum was deconvoluted into four peaks representing pyridinic (398.5 eV), pyrrolic (400.9 eV), graphitic (402.5 eV), and oxygenated (405.1 eV) N. The especially high pyridinic and pyrrolic N contents are desirable, because these N-containing species are capable of coordinating with Fe to form Fe–N_x moieties and thus are generally considered to be ORR active [6, 15, 43].

To confirm the enhanced active site accessibility, N_2 sorption analysis was performed on the Fe/Fe_3C@N-rGO aerogel catalyst and compared to catalysts obtained via the direct pyrolysis of PB (Fe/Fe_3C) and PB@GO (Fe/Fe_3C-rGO, without hydrothermal assembly). The Brunauer–Emmett–Teller (BET) surface area and pore distribution data is summarized in Table S1 (in the ESM). The BET surface area of Fe/Fe_3C was ~60.8 m^2/g, while that of Fe/Fe_3C-rGO was ~75.4 m^2/g. The improvement was only moderate, indicating severe rGO restacking during thermal treatment. However, as can be seen from Fig. 2(e), the Fe/Fe_3C@N-rGO aerogel displayed a type IV isotherm, which is characteristic of mesoporous materials. The BET surface area of the Fe/Fe_3C@N-rGO aerogel increased to 380 m^2/g, which was more than 5 times the value of Fe/Fe_3C-rGO, together with much greater pore area and pore volume. Such differences indicate the effectiveness of the aerogel structure in preventing GO restacking during pyrolysis. Although the rich macropores of the aerogel catalyst did not significantly contribute to the BET surface area, they are of paramount importance in expediting electrolyte filling and mass transport [44]. The SEM images of the directly pyrolyzed PB nanocubes (Fe/Fe_3C) and PB@GO (Fe/Fe_3C-rGO), from which apparent particle agglomeration was observed, further confirm the above discussion (Figs. S6 and S7 in the ESM). A more direct characterization of the catalytic active site accessibility was carried out through ECSA measurements, which can be estimated from the electrochemical double-layer capacitance (EDLC). As indicated in Fig. S8 (in the ESM), Fe/Fe_3C@rGO had a larger EDLC (2.63 mF/cm^2) compared to its directly pyrolyzed counterparts (1.35 mF/cm^2 for Fe/Fe_3C and 1.73 mF/cm^2 for Fe/Fe_3C-rGO), which corroborated the N_2 adsorption study. The N-doped aerogel catalysts possessed an even higher EDLC (4.23 mF/cm^2), which could be explained by the enhanced binding between N atoms in the rGO basal plane and electrolyte ions [45]. Therefore, the N-doped aerogel structure likely offers a porous, interconnected 3D network that can efficiently improve the active site accessibility and mass transport capability of the ORR catalyst.

Fundamental characterization of the as-obtained Fe/Fe_3C@N-rGO catalyst revealed numerous characteristics desirable for the ORR, including uniformly distributed catalyst nanoparticles, conformal graphitic carbon protecting shells, ample N-doping, and greatly enhanced active site accessibility. In order to evaluate the performance of the catalyst in the ORR, linear scanning voltammetry (LSV) curves were measured first on a RDE in 0.1 M KOH. As shown in Fig. 3(a), the rGO aerogel alone exhibited a low onset potential (0.84 V vs. RHE at 0.1 mA/cm^2) and low current density, probably due to the lack of effective intrinsic active sites [31]. Similarly, Fe/Fe_3C obtained from the direct pyrolysis of PB nanoparticles showed only mediocre activity, which could be attributed to the comparatively low accessible active site density caused by material agglomeration and the limited conductivity of Fe/Fe_3C. However, an obvious improvement in the catalytic performance, especially in terms of current density, was observed when the two were coupled together by physical mixing (Fe/Fe_3C+rGO), thanks to the high electron conductivity of rGO. In accord with our expectations, the aerogel catalyst exhibited an even more positive onset potential (0.91 V vs. RHE) and an improved current density. The best ORR performance was achieved by the N-doped aerogel catalyst (Fe/Fe_3C@N-rGO), with an onset potential of 0.95 V and a half-wave potential of 0.82 V. This performance was on par with the commercial Pt/C benchmark (Fuel Cell Store) even at the same mass loading, which is rather remarkable (Table S2 in the ESM). In order to gain further insight into the ORR kinetics, the electron transfer number (n) was calculated by the Koutecky–Levich (K–L) equation, which yielded n ~ 4.0. Therefore, the catalyst favors a desirable four-electron oxygen reduction pathway, similar to that of Pt/C. In addition, the Fe/Fe_3C@N-rGO showed a Tafel slope (78 mV/decade), which was comparable to that

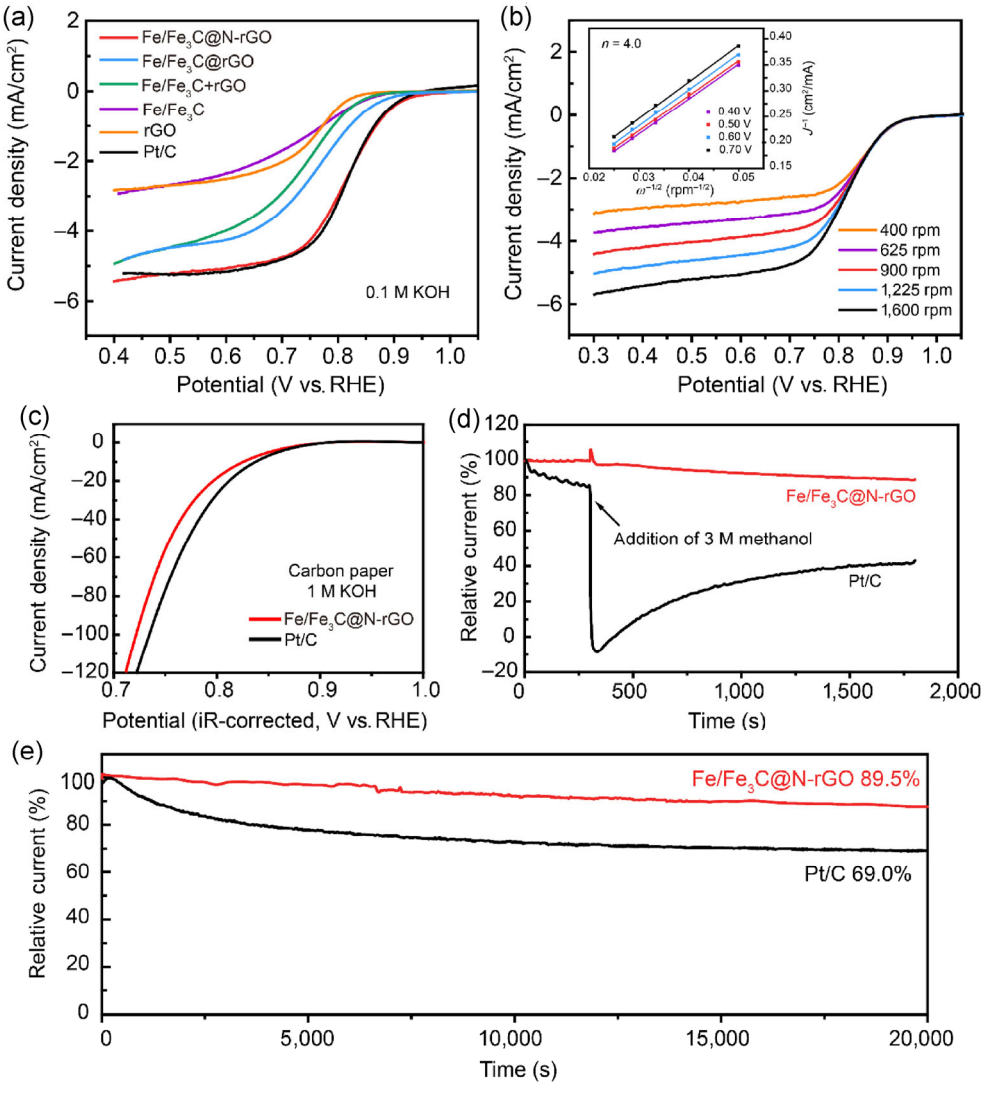

Figure 3 (a) RDE voltammograms of various ORR catalysts in O_2-saturated 0.1 M KOH at a rotation speed of 1,600 rpm (potential sweep rate 5 mV/s). The catalyst loading was 0.15 mg/cm^2 for all samples. (b) ORR polarization curves of Fe/Fe_3C@N-rGO at various rotating rates. The inset shows the corresponding K–L plots. (c) ORR polarization curves of Fe/Fe_3C@N-rGO and Pt/C on CFP in O_2-saturated 1 M KOH. The catalyst loading was 0.25 mg/cm^2. (d) Methanol tolerance experiment with the addition of 3 M methanol to O_2-saturated 0.1 M KOH at 0.7 V vs. RHE (rotation speed = 1,600 rpm). (e) Chronoamperometric responses of the catalysts at 0.7 V vs. RHE (rotation speed = 1,600 rpm).

of Pt/C (73 mV/decade), indicating good reaction kinetics.

To investigate the catalytic properties of the developed catalyst in a setting similar to that in fuel cells, we loaded the catalyst on Teflon-treated carbon fiber paper (CFP, Fuel Cell Store Toray Paper 060) and measured the iR-corrected polarization curves. In 1 M KOH, Fe/Fe_3C@N-rGO exhibited a similar performance to that of Pt/C (Fig. 3(c)), indicating the feasibility of the catalyst for real applications. The tolerance of cathode catalysts towards methanol crossover also plays a pivotal role in the commercialization of fuel cells. As shown in Fig. 3(d), after the injection of methanol, Fe/Fe_3C@N-rGO exhibited minimal alteration in the ORR current, while that of Pt/C drastically changed due methanol oxidation. Therefore, the developed catalyst exhibited superior electrocatalytic selectivity towards the ORR. Finally, the durability of Fe/Fe_3C@N-rGO and Pt/C was compared by chronoamperometric measurements at 0.7 V vs. RHE in O_2-saturated 0.1 M KOH. After 20,000 s, Fe/Fe_3C@N-rGO retained up to 89.5% of its initial current, while that of Pt/C decreased

by more than 31% under the same experimental conditions.

The aforementioned electrochemical characterization can serve as strong evidence of the effectiveness of the proposed PB 3D aerogel design in enhancing the accessible active site density and thus the electrocatalytic performance of M–N/C catalysts. Nevertheless, the exact roles of each component in Fe/Fe_3C@N-rGO in the ORR remain to be elucidated. Therefore, further experiments were carried out in order to obtain a deeper understanding. First, in order to clarify the function of Fe and Fe_3C, chemically unstable metallic Fe species were selectively removed by vigorous acid leaching as confirmed by XRD (Fig. 4(a)). However, the acid leaching process did not significantly alter the electrochemical performance of the catalyst, despite a slight decrease in the diffusion-limited current density (Fig. 4(b)). This suggests that Fe, or more precisely, free metallic Fe species, may not be necessary for improving the ORR performance [39, 46]. Notably, the acid-leached aerogel catalyst also exhibited promising ORR activity in acidic media (Fig. S11 in the ESM). Although the onset potential decreased below that of Pt/C in O_2-saturated 0.05 M H_2SO_4, the limiting current

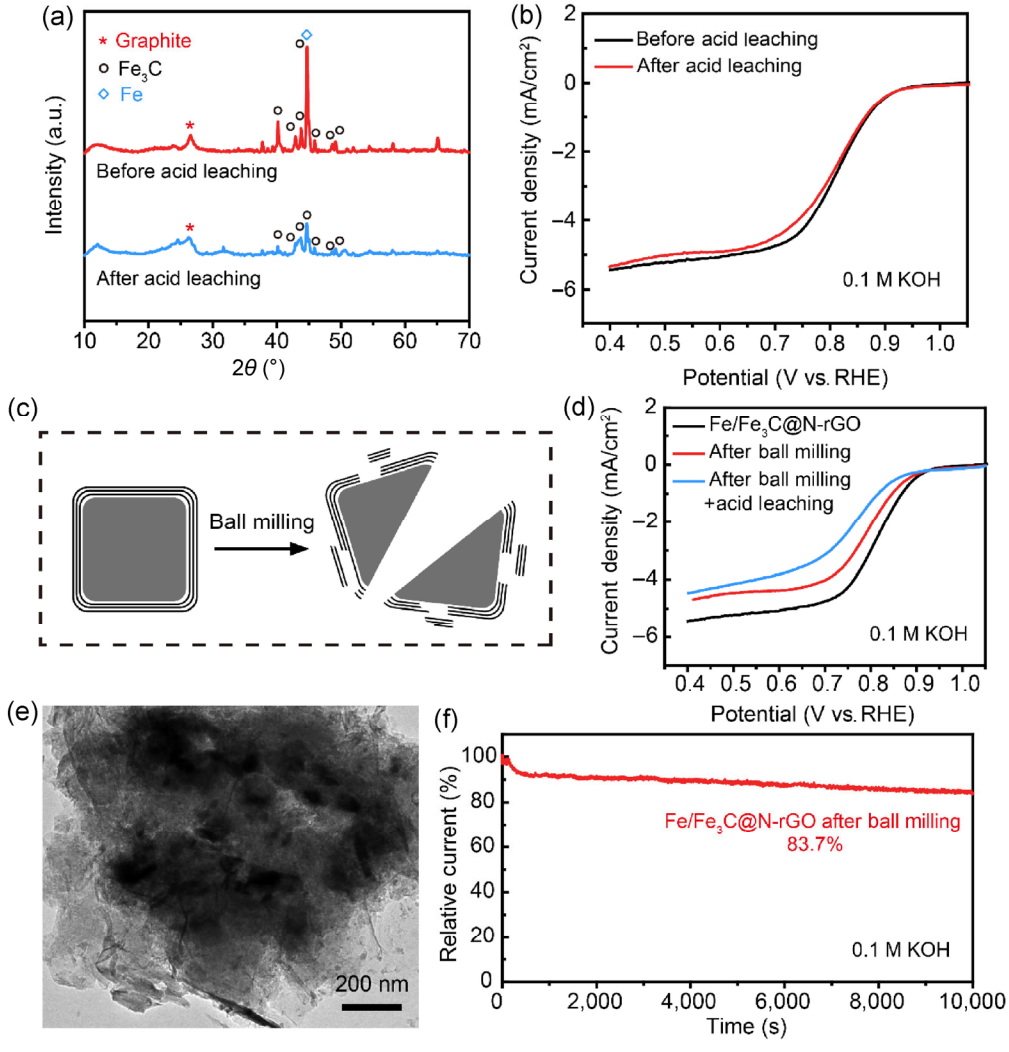

Figure 4 (a) XRD spectra of the Fe/Fe_3C@N-rGO catalyst before and after acid etching, which demonstrate successful removal of metallic Fe. (b) ORR polarization curves of Fe/Fe_3C@N-rGO before and after acid leaching. (c) Schematic illustration of the effect of ball milling on the aerogel catalyst. Ball milling can not only break apart the Fe_3C core, but also detach the graphitic carbon shell from the Fe_3C surface. (d) ORR polarization curves of Fe/Fe_3C@N-rGO, ball-milled Fe/Fe_3C@N-rGO, and ball-milled Fe/Fe_3C@N-rGO after acid leaching. (e) TEM image of ball-milled Fe/Fe_3C@N-rGO. (f) Chronoamperometric responses of ball-milled Fe/Fe_3C@N-rGO at 0.7 V vs. RHE (rotation speed = 1,600 rpm).

(6.2 mA/cm^2 at 0.3 V) was much higher than that of Pt/C (5.7 mA/cm^2 at 0.3 V) and it exhibited superior long-term stability.

As for Fe_3C, the Fe_3C nanoparticles were encapsulated within the graphitic carbon shell and, thus, were not in direct contact with the electrolyte. Therefore, the function of Fe_3C is debatable. Encapsulated Fe_3C can likely modify the electron density of the surrounding graphitic carbon, promoting charge transfer from carbon to O_2; in turn, the carbon shell would enhance the interfacial contact, and suppress Fe_3C dissolution and agglomeration in the electrolyte [27, 39, 47]. To verify the synergistic effect of encapsulated Fe_3C and the graphitic carbon shell, Fe/Fe_3C@N-rGO was subjected to high-energy ball milling, the effect of which is schematically illustrated in Fig. 4(c). Ball milling can break apart the Fe_3C particles and destroy the protective carbon shells around them, as revealed by TEM (Fig. 4(e)). After milling, an apparent negative shift in the onset potential and a decrease in the current density were observed (Fig. 4(d)), probably due to the disruption of the contact between graphitic carbon and Fe_3C. Moreover, the Fe_3C nanoparticles were exposed and therefore soluble in hot acid after milling. As a result, the ball-milled sample exhibited an even worse ORR performance after acid leaching, due to the removal of Fe_3C, which could no longer activate the surrounding carbon. Correspondingly, the ball-milled aerogel catalyst displayed deteriorated stability (Fig. 4(f)), with merely 83.7% current retention after only 10,000 s (compared to 89.5% current retention after 20,000 s for the original sample). In addition, the fact that the aerogel catalysts greatly outperformed the physically mixed counterpart also supported the importance of good graphitic carbon-Fe_3C electrical contact in ORR catalysis. Thus, although Fe_3C nanoparticles are not in direct contact with O_2, they still play an important role in ORR catalysis, which is most likely defined as a host–guest interaction with the surrounding protective carbon layers. Finally, in regard to the function of N-doped rGO, the doping of carbon-based materials with heteroatoms such as N could easily shift the electron neutrality of adjacent carbon atoms and create positively charged sites, favoring O_2 adsorption and reduction [47], in addition to the formation of ORR-active Fe–N_x moieties.

3 Conclusions

In conclusion, we have successfully developed a facile route to obtain 3D Fe/Fe_3C N-doped graphene aerogel ORR electrocatalysts with a hierarchical pore system. PB is an ideal precursor to obtain the M–N/C catalyst due to its large surface area, high-density Fe–N_4 coordination sites, and low cost. By directly anchoring PB nanoparticles on GO followed by hydrothermal assembly, particle agglomeration during the subsequent pyrolysis step can be effectively hampered, affording a catalyst with numerous catalytic centers of high intrinsic activity, and greatly enhanced active site density and accessibility. The obtained Fe/Fe_3C@N-rGO catalyst displayed excellent ORR activity on par with that of the state-of-the-art Pt/C catalyst in alkaline media at the same mass loading and outstanding ORR activity in acidic media along with remarkable stability and methanol crossover tolerance, which was among the best nonprecious-metal ORR catalysts reported to date. In addition, we found that Fe_3C was important for ORR catalysis, owing to its synergistic effects with graphitic carbon. Although it is not in direct contact with the electrolyte, Fe_3C may activate the surrounding graphitic carbon layers towards ORR; in turn, the protecting carbon shells enabled rapid shuttling of charges and protected the Fe_3C cores from dissolution and agglomeration during operation. The PB-derived aerogel catalyst with enhanced active site accessibility will shed light on novel design principles for the efficient synthesis of nonprecious-metal electrocatalysts. Given the variety of MOF-based structures, this approach could be widely adopted to generate tailored materials for various catalytic applications.

Acknowledgments

We acknowledge the support from Global Climate and Energy Projects (GCEP) at Stanford University.

Electronic Supplementary Material: Supplementary material (experimental details and supplementary figures) is available in the online version of this article at http://dx.doi.org/10.1007/s12274-016-1300-x.

References

[1] Wu, G.; Zelenay, P. Nanostructured nonprecious metal catalysts for oxygen reduction reaction. *Acc. Chem. Res.* **2013**, *46*, 1878–1889.

[2] Lefèvre, M.; Proietti, E.; Jaouen, F.; Dodelet, J. P. Iron-based catalysts with improved oxygen reduction activity in polymer electrolyte fuel cells. *Science* **2009**, *324*, 71–74.

[3] Debe, M. K. Electrocatalyst approaches and challenges for automotive fuel cells. *Nature* **2012**, *486*, 43–51.

[4] Wang, Z. L.; Xu, D.; Xu, J. J.; Zhang, X. B. Oxygen electrocatalysts in metal-air batteries: From aqueous to nonaqueous electrolytes. *Chem. Soc. Rev.* **2014**, *43*, 7746–7786.

[5] Huang, X. Q.; Zhao, Z. P.; Cao, L.; Chen, Y.; Zhu, E. B.; Lin, Z. Y.; Li, M. F.; Yan, A. M.; Zettl, A.; Wang, Y. M. et al. High-performance transition metal-doped Pt_3Ni octahedra for oxygen reduction reaction. *Science* **2015**, *348*, 1230–1234.

[6] Chen, Z. W.; Higgins, D.; Yu, A. P.; Zhang, L.; Zhang, J. J. A review on non-precious metal electrocatalysts for PEM fuel cells. *Energy Environ. Sci.* **2011**, *4*, 3167–3192.

[7] Chung, D. Y.; Kim, H. I.; Chung, Y. H.; Lee, M. J.; Yoo, S. J.; Bokare, A. D.; Choi, W.; Sung, Y. E. Inhibition of CO poisoning on Pt catalyst coupled with the reduction of toxic hexavalent chromium in a dual-functional fuel cell. *Sci. Rep.* **2014**, *4*, 7450.

[8] Ma, X. M.; Meng, H.; Cai, M.; Shen, P. K. Bimetallic carbide nanocomposite enhanced Pt catalyst with high activity and stability for the oxygen reduction reaction. *J. Am. Chem. Soc.* **2012**, *134*, 1954–1957.

[9] Yin, H. J.; Tang, H. J.; Wang, D.; Gao, Y.; Tang, Z. Y. Facile synthesis of surfactant-free Au cluster/graphene hybrids for high-performance oxygen reduction reaction. *ACS Nano* **2012**, *6*, 8288–8297.

[10] Zhao, S. L.; Yin, H. J.; Du, L.; Yin, G. P.; Tang, Z. Y.; Liu, S. Q. Three dimensional N-doped graphene/PtRu nanoparticle hybrids as high performance anode for direct methanol fuel cells. *J. Mater. Chem. A* **2014**, *2*, 3719–3724.

[11] Zhou, R. F.; Qiao, S. Z. An Fe/N co-doped graphitic carbon bulb for high-performance oxygen reduction reaction. *Chem. Commun.* **2015**, *51*, 7516–7519.

[12] Zhang, J. T.; Zhao, Z. H.; Xia, Z. H.; Dai, L. M. A metal-free bifunctional electrocatalyst for oxygen reduction and oxygen evolution reactions. *Nat. Nanotechnol.* **2015**, *10*, 444–452.

[13] Wu, Z. S.; Chen, L.; Liu, J. Z.; Parvez, K.; Liang, H. W.; Shu, J.; Sachdev, H.; Graf, R.; Feng, X. L.; Müllen, K. High-performance electrocatalysts for oxygen reduction derived from cobalt porphyrin-based conjugated mesoporous polymers. *Adv. Mater.* **2014**, *26*, 1450–1455.

[14] Lin, L.; Zhu, Q.; Xu, A. W. Noble-metal-free Fe-N/C catalyst for highly efficient oxygen reduction reaction under both alkaline and acidic conditions. *J. Am. Chem. Soc.* **2014**, *136*, 11027–11033.

[15] Niu, W. H.; Li, L. G.; Liu, X. J.; Wang, N.; Liu, J.; Zhou, W. J.; Tang, Z. H.; Chen, S. W. Mesoporous N-doped carbons prepared with thermally removable nanoparticle templates: An efficient electrocatalyst for oxygen reduction reaction. *J. Am. Chem. Soc.* **2015**, *137*, 5555–5562.

[16] Ma, R. G.; Ren, X. D.; Xia, B. Y.; Zhou, Y.; Sun, C.; Liu, Q.; Liu, J. J.; Wang, J. C. Novel synthesis of N-doped graphene as an efficient electrocatalyst towards oxygen reduction. *Nano Res.* **2016**, *9*, 808–819.

[17] Lei, Y. P.; Shi, Q.; Han, C.; Wang, B.; Wu, N.; Wang, H.; Wang, Y. D. N-doped graphene grown on silk cocoon-derived interconnected carbon fibers for oxygen reduction reaction and photocatalytic hydrogen production. *Nano Res.* **2016**, *9*, 2498–2509.

[18] Liu, Z. Y.; Zhang, G. X.; Lu, Z. Y.; Jin, X. Y.; Chang, Z.; Sun, X. M. One-step scalable preparation of N-doped nano-porous carbon as a high-performance electrocatalyst for the oxygen reduction reaction. *Nano Res.* **2013**, *6*, 293–301.

[19] Liang, Y. Y.; Li, Y. G.; Wang, H. L.; Zhou, J. G.; Wang, J.; Regier, T.; Dai, H. J. Co_3O_4 nanocrystals on graphene as a synergistic catalyst for oxygen reduction reaction. *Nat. Mater.* **2011**, *10*, 780–786.

[20] Xia, W.; Zou, R. Q.; An, L.; Xia, D. G.; Guo, S. J. A metal-organic framework route to *in situ* encapsulation of $Co@Co_3O_4@C$ core@bishell nanoparticles into a highly ordered porous carbon matrix for oxygen reduction. *Energy Environ. Sci.* **2015**, *8*, 568–576.

[21] Wu, Z.-S.; Yang, S. B.; Sun, Y.; Parvez, K.; Feng, X. L.; Müllen, K. 3D nitrogen-doped graphene aerogel-supported Fe_3O_4 nanoparticles as efficient electrocatalysts for the oxygen reduction reaction. *J. Am. Chem. Soc.* **2012**, *134*, 9082–9085.

[22] Fu, G. T.; Liu, Z. Y.; Zhang, J. F.; Wu, J. Y.; Xu, L.; Sun, D. M.; Zhang, J. B.; Tang, Y. W.; Chen, P. Spinel $MnCo_2O_4$ nanoparticles cross-linked with two-dimensional porous carbon nanosheets as a high-efficiency oxygen reduction electrocatalyst. *Nano Res.* **2016**, *9*, 2110–2122.

[23] Wei, P. J.; Yu, G. Q.; Naruta, Y.; Liu, J. G. Covalent grafting of carbon nanotubes with a biomimetic heme model compound to enhance oxygen reduction reactions. *Angew. Chem., Int. Ed.* **2014**, *53*, 6659–6663.

[24] Cao, R. G.; Thapa, R.; Kim, H.; Xu, X. D.; Kim, M. G.; Li, Q.; Park, N.; Liu, M. L.; Cho, J. Promotion of oxygen reduction by a bio-inspired tethered iron phthalocyanine carbon nanotube-based catalyst. *Nat. Commun.* **2013**, *4*, 2076.

[25] Tang, H. J.; Yin, H. J.; Wang, J. Y.; Yang, N. L.; Wang, D.;

Tang, Z. Y. Molecular architecture of cobalt porphyrin multilayers on reduced graphene oxide sheets for high-performance oxygen reduction reaction. *Angew. Chem., Int. Ed.* **2013**, *52*, 5585–5589.

[26] Wu, G.; More, K. L.; Johnston, C. M.; Zelenay, P. High-performance electrocatalysts for oxygen reduction derived from polyaniline, iron, and cobalt. *Science* **2011**, *332*, 443–447.

[27] Hu, Y.; Jensen, J. O.; Zhang, W.; Cleemann, L. N.; Xing, W.; Bjerrum, N. J.; Li, Q. F. Hollow spheres of iron carbide nanoparticles encased in graphitic layers as oxygen reduction catalysts. *Angew. Chem., Int. Ed.* **2014**, *53*, 3675–3679.

[28] Xiao, M. L.; Zhu, J. B.; Feng, L. G.; Liu, C. P.; Xing, W. Meso/macroporous nitrogen-doped carbon architectures with iron carbide encapsulated in graphitic layers as an efficient and robust catalyst for the oxygen reduction reaction in both acidic and alkaline solutions. *Adv. Mater.* **2015**, *27*, 2521–2527.

[29] Zhao, D.; Shui, J. L.; Chen, C.; Chen, X. Q.; Reprogle, B. M.; Wang, D. P.; Liu, D. J. Iron imidazolate framework as precursor for electrocatalysts in polymer electrolyte membrane fuel cells. *Chem. Sci.* **2012**, *3*, 3200–3205.

[30] Lee, J. S.; Park, G. S.; Kim, S. T.; Liu, M. L.; Cho, J. A highly efficient electrocatalyst for the oxygen reduction reaction: N-doped ketjenblack incorporated into Fe/Fe_3C-functionalized melamine foam. *Angew. Chem. Int. Ed.* **2013**, *52*, 1026–1030.

[31] Wu, Z. Y.; Xu, X. X.; Hu, B. C.; Liang, H. W.; Lin, Y.; Chen, L. F.; Yu, S. H. Iron carbide nanoparticles encapsulated in mesoporous Fe-N-doped carbon nanofibers for efficient electrocatalysis. *Angew. Chem., Int. Ed.* **2015**, *54*, 8179–8183.

[32] Zhang, S. M.; Zhang, H. Y.; Liu, Q.; Chen, S. L. Fe-N doped carbon nanotube/graphene composite: Facile synthesis and superior electrocatalytic activity. *J. Mater. Chem. A* **2013**, *1*, 3302–3308.

[33] Masa, J.; Xia, W.; Muhler, M.; Schuhmann, W. On the role of metals in nitrogen-doped carbon electrocatalysts for oxygen reduction. *Angew. Chem., Int. Ed.* **2015**, *54*, 10102–10120.

[34] Huang, H.; Feng, X.; Du, C. C.; Wu, S. Y.; Song, W. B. One-step pyrolytic synthesis of small iron carbide nano-particles/3D porous nitrogen-rich graphene for efficient electrocatalysis. *J. Mater. Chem. A* **2015**, *3*, 4976–4982.

[35] Pintado, S.; Goberna-Ferrón, S.; Escudero-Adán, E. C.; Galán-Mascarós, J. R. Fast and persistent electrocatalytic water oxidation by Co-Fe Prussian blue coordination polymers. *J. Am. Chem. Soc.* **2013**, *135*, 13270–13273.

[36] Lee, J. S.; Nam, G.; Sun, J.; Higashi, S.; Lee, H. W.; Lee, S.; Chen, W.; Cui, Y.; Cho, J. Composites of a Prussian blue analogue and gelatin-derived nitrogen-doped carbon-supported porous spinel oxides as electrocatalysts for a Zn–air battery. *Adv. Energy Mater.,* in press, DOI: 10.1002/aenm.201601052.

[37] Xia, W.; Mahmood, A.; Zou, R. Q.; Xu, Q. Metal-organic frameworks and their derived nanostructures for electrochemical energy storage and conversion. *Energ. Environ. Sci.* **2015**, *8*, 1837–1866.

[38] Zhao, S. L.; Yin, H. J.; Du, L.; He, L. C.; Zhao, K.; Chang, L.; Yin, G. P.; Zhao, H. J.; Liu, S. Q.; Tang, Z. Y. Carbonized nanoscale metal-organic frameworks as high performance electrocatalyst for oxygen reduction reaction. *ACS Nano* **2014**, *8*, 12660–12668.

[39] Hou, Y.; Huang, T. Z.; Wen, Z. H.; Mao, S.; Cui, S. M.; Chen, J. H. Metal−organic framework-derived nitrogen-doped core–shell-structured porous Fe/Fe_3C@C nanoboxes supported on graphene sheets for efficient oxygen reduction reactions. *Adv. Energy Mater.* **2014**, *4*, 1400337.

[40] Ma, T. Y.; Dai, S.; Jaroniec, M.; Qiao, S. Z. Metal-organic framework derived hybrid Co_3O_4-carbon porous nanowire arrays as reversible oxygen evolution electrodes. *J. Am. Chem. Soc.* **2014**, *136*, 13925–13931.

[41] Mao, S.; Lu, G. H.; Chen, J. H. Three-dimensional graphene-based composites for energy applications. *Nanoscale* **2015**, *7*, 6924–6943.

[42] Kong, B. A.; Sun, X. T.; Selomulya, C.; Tang, J.; Zheng, G. F.; Wang, Y. Q.; Zhao, D. Y. Sub-5 nm porous nanocrystals: Interfacial site-directed growth on graphene for efficient biocatalysis. *Chem. Sci.* **2015**, *6*, 4029–4034.

[43] Cui, X. Y.; Yang, S. B.; Yan, X. X.; Leng, J. G.; Shuang, S.; Ajayan, P. M.; Zhang, Z. J. Pyridinic-nitrogen-dominated graphene aerogels with Fe–N–C coordination for highly efficient oxygen reduction reaction. *Adv. Funct. Mater.* **2016**, *26*, 5708–5717.

[44] Xu, J. B.; Zhao, T. S. Mesoporous carbon with uniquely combined electrochemical and mass transport characteristics for polymer electrolyte membrane fuel cells. *RSC Adv.* **2013**, *3*, 16–24.

[45] Jeong, H. M.; Lee, J. W.; Shin, W. H.; Choi, Y. J.; Shin, H. J.; Kang, J. K.; Choi, J. W. Nitrogen-doped graphene for high-performance ultracapacitors and the importance of nitrogen-doped sites at basal planes. *Nano Lett.* **2011**, *11*, 2472–2477.

[46] Kobayashi, M.; Niwa, H.; Saito, M.; Harada, Y.; Oshima, M.; Ofuchi, H.; Terakura, K.; Ikeda, T.; Koshigoe, Y.; Ozaki, J. et al. Indirect contribution of transition metal towards oxygen reduction reaction activity in iron phthalocyanine-based carbon catalysts for polymer electrolyte fuel cells. *Electrochim. Acta* **2012**, *74*, 254–259.

[47] Deng, D. H.; Yu, L.; Chen, X. Q.; Wang, G. X.; Jin, L.; Pan, X. L.; Deng, J.; Sun, G. Q.; Bao, X. H. Iron encapsulated within pod-like carbon nanotubes for oxygen reduction reaction. *Angew. Chem., Int. Ed.* **2013**, *52*, 371–375.